Neutron matter in the hole-line expansion

Jia-Jing Lu (陆家靖), Zeng-Hua Li (李增花),* and Chong-Yang Chen (陈重阳)
Key Laboratory of Nuclear Physics and Ion-beam Application (MOE), Institute of Modern Physics, Fudan University, Shanghai 200433, People's Republic of China

M. Baldo and H.-J. Schulze
Dipartimento di Fisica, INFN Sezione di Catania, Universitá di Catania, Via Santa Sofia 64, 95123 Catania, Italy

(Received 25 July 2018; revised manuscript received 25 September 2018; published 26 December 2018)

We calculate the binding energy of pure neutron matter up to third order in the Brueckner-Bethe-Goldstone hole-line expansion, employing various modern nucleon-nucleon potentials. At that order all results appear well converged to within a few percent up to a density of 0.8 fm^{-3}. We analyze the potentials in terms of the strength of their hard core. Comparison with results of other theoretical methods is made.

DOI: 10.1103/PhysRevC.98.064322

I. INTRODUCTION

The idealized environment of strongly interacting pure neutron matter (PNM) has always represented a benchmark scenario to test theoretical many-body methods and models for the nucleon-nucleon (NN) interaction [1], apart from its importance for the physics of neutron stars [2]. This is because the interaction is weaker in this system compared to symmetric nuclear matter (SNM), mainly due to the absence of the dominant very strong interaction in the $^3SD_1$ channel. This renders PNM in general more accessible to various theoretical many-body methods.

We have recently analyzed SNM [3,4] in the Brueckner-Bethe-Goldstone expansion [5–7] with particular attention to newly developed chiral potentials [8], and demonstrated that the binding energy per particle appears well converged at third order in the hole-line parameter κ. Qualitative differences between traditional hard-core meson-exchange-inspired potentials and the soft-core chiral potentials have been pointed out, namely the wound parameter κ is naturally larger in the former case, which is correlated to saturation of SNM at smaller density and less binding. In any case the saturation points keep lying on the Coester band [9,10] and good saturation of SNM cannot be achieved without considering three-nucleon forces, which have to be rather strong for the soft-core NN potentials.

The purpose of the present paper is to extend this analysis to PNM, and investigate the differences between hard-core and soft-core potentials in the same manner. We thus compute the binding energy per nucleon in the hole-line expansion (HLE),

$$B/A = T + E_2 + E_3 + \ldots, \tag{1}$$

where T is the kinetic energy, $E_2 = E_{\rm BHF}$ is the two-hole-line (2HL) contribution at Brueckner-Hartree-Fock (BHF) level, and E_3 is the three-hole-line (3HL) contribution, which will be the main focus of this paper. Since a consistent theory of 3HL contributions and three-nucleon forces is not yet available, we perform here the standard analysis of the HLE based on two-nucleon forces only.

In Refs. [3,4] we employed the Argonne V18 [11], the CDBONN [12], and the N3LO chiral potentials [13] with two values of the chiral cutoff $\Lambda = 450, 500$ MeV. In the meantime N4LO chiral potentials of the same (EM) family have appeared [14] for cutoff values $\Lambda = 450, 500, 550$ MeV, which will also be analyzed in this work.

II. FORMALISM

We only briefly repeat here the essential points of the formalism, which is exposed in detail in Refs. [3,4,6,15]. The HLE parameter κ can be defined in several equivalent ways, in particular from the depletion of the physical momentum distribution $n(k)$,

$$\kappa \equiv \sum_{k<k_F}[1-n(k)] \Big/ \sum_{k<k_F} n_0(k) = \sum_{k>k_F} n(k) \Big/ \sum_{k<k_F} n_0(k), \tag{2}$$

where $n_0(k) = \theta(k_F - k)$ is the occupation number for the free Fermi gas, or from the wound of the NN defect function $\eta(r)$ [4,16–18],

$$\kappa = \rho \int d^3\boldsymbol{r} \langle |\eta(\boldsymbol{r})|^2 \rangle_{S,T} \equiv \frac{V_{\rm core}}{V/N} = \left(\frac{c}{d}\right)^3, \tag{3}$$

which expresses most clearly the correlation parameter as the ratio of the (hard-)core volume to the volume per particle, or equivalently, the cubed ratio of core diameter c to average nucleon distance d. Since the core volume or diameter defined in this way from the density-dependent defect functions are not constant, but in general shrink with increasing density,

*zhli09@fudan.edu.cn

the result is a nonlinear density dependence of the correlation parameter κ.

We stress that both definitions Eqs. (2) and (3) are equivalent under certain approximations, see, e.g., the derivation in Ref. [3]. In particular, the approximation $Q^2 \approx Q$ for the angle-averaged Pauli operator appearing in Eq. (12) is used. This implies values typically 20% smaller predicted by Eq. (3), but qualitative conclusion are not affected.

At the 2HL level of approximation the energy per particle of nuclear matter in Eq. (1) is given by

$$E_2 = \frac{1}{2A}\sum_{12} n_0(1)n_0(2)\langle 12|G(e_1+e_2)|12\rangle, \qquad (4)$$

where each variable $1,\ldots$ stands for $(\boldsymbol{k},\sigma,\tau)_1$, i.e., the three-dimensional momentum $\boldsymbol{k}$ and the spin-isospin variables σ,τ. Antisymmetrization of the matrix elements is always understood. In the BBG expansion the bare NN two-body interaction V is systematically replaced by the G matrix, which satisfies the Bethe-Goldstone equation

$$\langle 12|G(W)|1'2'\rangle = \langle 12|V|1'2'\rangle - \sum_{1''2''}\langle 12|V|1''2''\rangle\frac{Q}{E-W}\langle 1''2''|G(W)|1'2'\rangle. \qquad (5)$$

The energy W is the so-called starting energy, which appears as a parameter in the equation. The Pauli operator Q projects the intermediate states $1'', 2''$ with energy $E = e_{1''} + e_{2''}$ above the Fermi momenta. As is well known, the G matrix sums up the ladder diagrams in the particle-particle scattering and takes into account most of the short-range correlations introduced by the hard core of the interaction, if present. It is therefore much softer than the original bare interaction and an expansion in terms of the G matrix is expected to have an improved rate of convergence [6].

This convergence rate also depends on the choice of the single-particle spectrum,

$$e_1 = \frac{k_1^2}{2m_1} + U(1)\,, \quad U(1) = \sum_2\langle 12|G(e_1+e_2)|12\rangle, \qquad (6)$$

which might be enforced for any momentum (continuous choice) or only for hole states, setting $U(k > k_F) \equiv 0$ (gap choice). Equations (5), (6) imply a self-consistent procedure for the calculation of the single-particle (s.p.) potential $U(k)$, which will then be used also to calculate the 3HL diagrams.

The computation of the 3HL energy E_3 is a considerable numerical effort, which involves evaluating different diagrammatic contributions visualized in Fig. 1,

$$E_3 = E_{\rm Bubble} + E_{\rm Ring} + E_{\rm Higher}, \qquad (7)$$

among which strong cancellations occur, typically between repulsive bubble and attractive ring+higher contributions. We refer to Refs. [4,6,15] for a complete documentation.

3HL PNM calculations have so far been performed for the Urbana V14 and Argonne V18 [19,20], the CDBONN [21], the Argonne V8,V6,V4 [22], and the fss2 [23] potentials. We now present our results for the N3LO(450,500) and N4LO(450,500,550) EM chiral potentials in comparison with the AV18 and CDBONN forces, which can be considered representative of highly accurate traditional meson-exchange-inspired potentials.

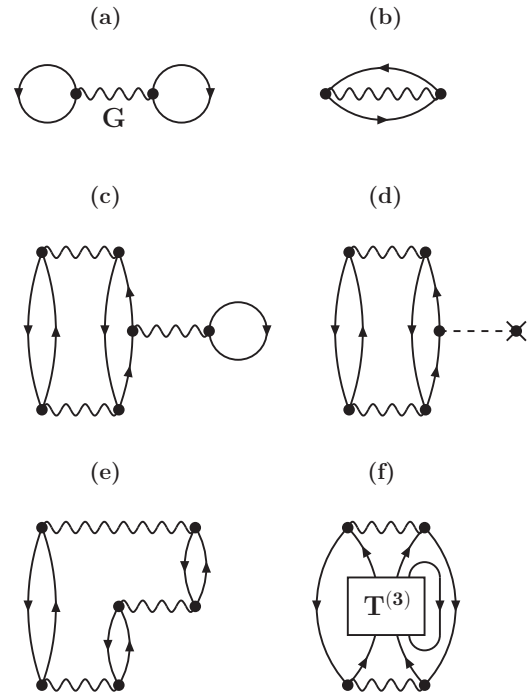

FIG. 1. Different Goldstone diagrams contributing to the binding energy of nuclear matter: Diagrams (a) and (b) correspond to the 2HL (BHF) calculation. The sum of the other diagrams, (c), (d) bubble, (e) ring, (f) higher, gives the 3HL contribution. $T^{(3)}$ is the three-body in-medium scattering matrix. For a detailed discussion, see Refs. [4,6,15].

III. RESULTS

A. Potential matrix elements

In order to have a first idea of the general characteristics of the different potentials, we examine in Fig. 2 the diagonal momentum-space potential matrix elements $V_{SJLL'}(k,k)$ in the most important $^1S_0$ and coupled $^3PF_2$ partial waves. In the case of r-space potentials they are defined as

$$V_{SJLL'}(k,k') = \int_0^\infty dr\, r^2 j_L(kr) V_{SJLL'}(r) j_{L'}(k'r). \qquad (8)$$

One notes immediately the qualitative difference between the meson-exchange potentials (AV18, CDBONN), which exhibit a pronounced hard-core tail at large momenta, and the chiral potentials, which are cut off around $k \approx 3$ fm^{-1}. The variation due to the different values of the chiral cutoff $\Lambda = 450, 500, 550$ MeV is also clearly evident. One may also note that the N3LO450 and N4LO450 interactions (and to some extend also N3LO500 and N4LO500) are actually very similar, which is also reflected in the results discussed in the following.

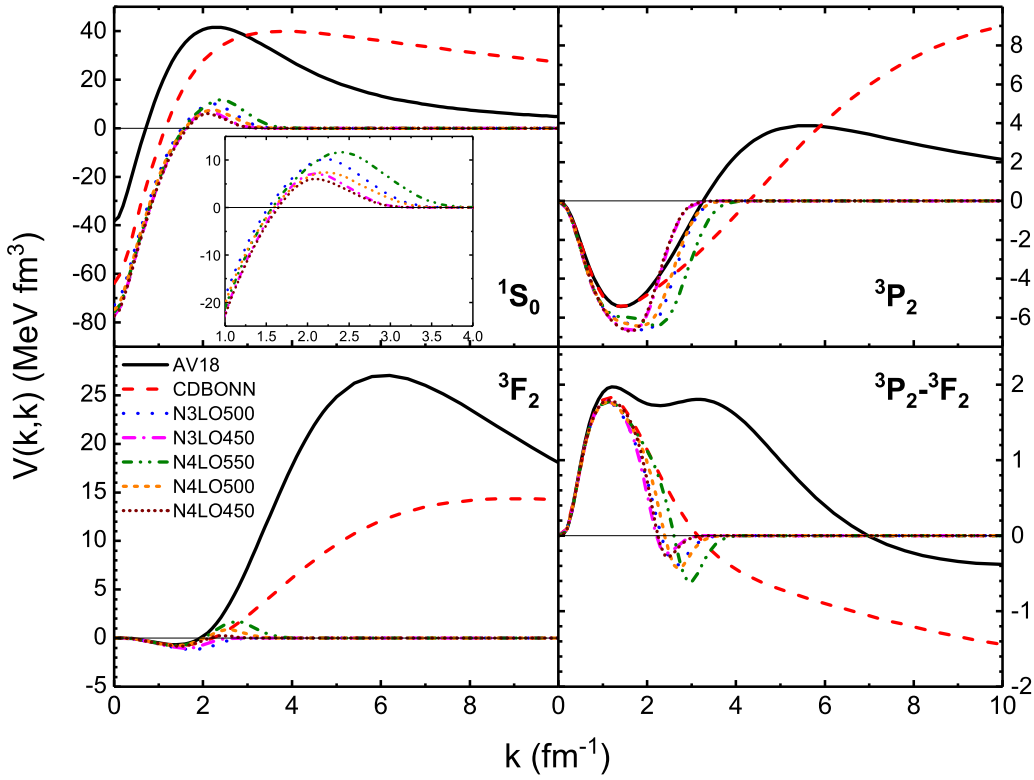

FIG. 2. Diagonal matrix element $V_{^1S_0}(k,k)$ and $V_{^3PF_2}(k,k)$ for various NN potentials. Note the different energy scales.

B. Momentum distribution

In BHF approximation the momentum distribution can be obtained from the mass operators M_1 and M_2 (BHF and rearrangement contributions to the s.p. potential) as [3,24–26]

$$n(k < k_F) = 1 + \left.\frac{\partial M_1(k,\omega)}{\partial\omega}\right|_{\omega=e_k}, \tag{9}$$

$$n(k > k_F) = -\left.\frac{\partial M_2(k,\omega)}{\partial\omega}\right|_{\omega=e_k}, \tag{10}$$

and the results for PNM are shown in Fig. 3, where the bottom panels show more clearly the long-range tails of the distributions by weighting with a factor k^2, which helps us to see clearly the discrepancy between various potentials at large momenta.

One observes that for the hard-core potentials, the deviations from the Fermi distribution increase with density due to increased excitation over the Fermi surface. This is not the case for the softest chiral potentials, which do not provide the necessary scattering amplitude at large momenta. The depletion of the momentum distribution is smaller than in SNM at the same density [3], due to the weaker overall interaction strength. (For example, the depletion with the AV18 at $k = 0$ is about 0.2 in that case, nearly density independent). This obviously implies also smaller values of the correlation parameter κ defined as average depletion, Eq. (2).

C. Defect functions

The r-space defect functions in the partial waves $\alpha = {}^1S_0, {}^3PF_2$,

$$\eta_\alpha(r) = j_\alpha(r) - u_\alpha(r) \tag{11}$$

$$= \int \frac{dq'\,q'^2}{2\pi^2} j_\alpha(q'r) \frac{Q(\bar{p},q')G_\alpha(\bar{p},\bar{q},q')}{E(\bar{p},\bar{q},q')}, \tag{12}$$

with the free wave function (Bessel function) j_α, the correlated wave function u_α, Pauli operator Q, energy denominator E, and G matrix evaluated at averaged total and relative momenta $\bar{p}, \bar{q}$ [3], are shown in Fig. 4 for different densities. In the dominant $^1S_0$ channel, the hard core of the meson-exchange potentials is clearly evident, whereas the defect of the chiral potentials diminishes with decreasing cutoff and with increasing density, consistent with the features of the momentum distributions in Fig. 3. This behavior is the same as in SNM, see Fig. 3 of Ref. [3].

The HLE condition $c < d$ is well fulfilled for all potentials and densities. This is not the case for the coupled $^3PF_2$ wave defect, which even at low density extends beyond the average particle distance d, in particular for chiral potentials with low cutoff. However, its overall magnitude is completely negligible compared to the $^1S_0$ wave. This is in contrast to SNM [3], where the $^3SD_1$ channel (absent in PNM) is actually dominant at low density and its competition with the other partial waves determines the overall density dependence of the total correlation parameter $\kappa = \sum_\alpha \kappa_\alpha$, which we discuss now.

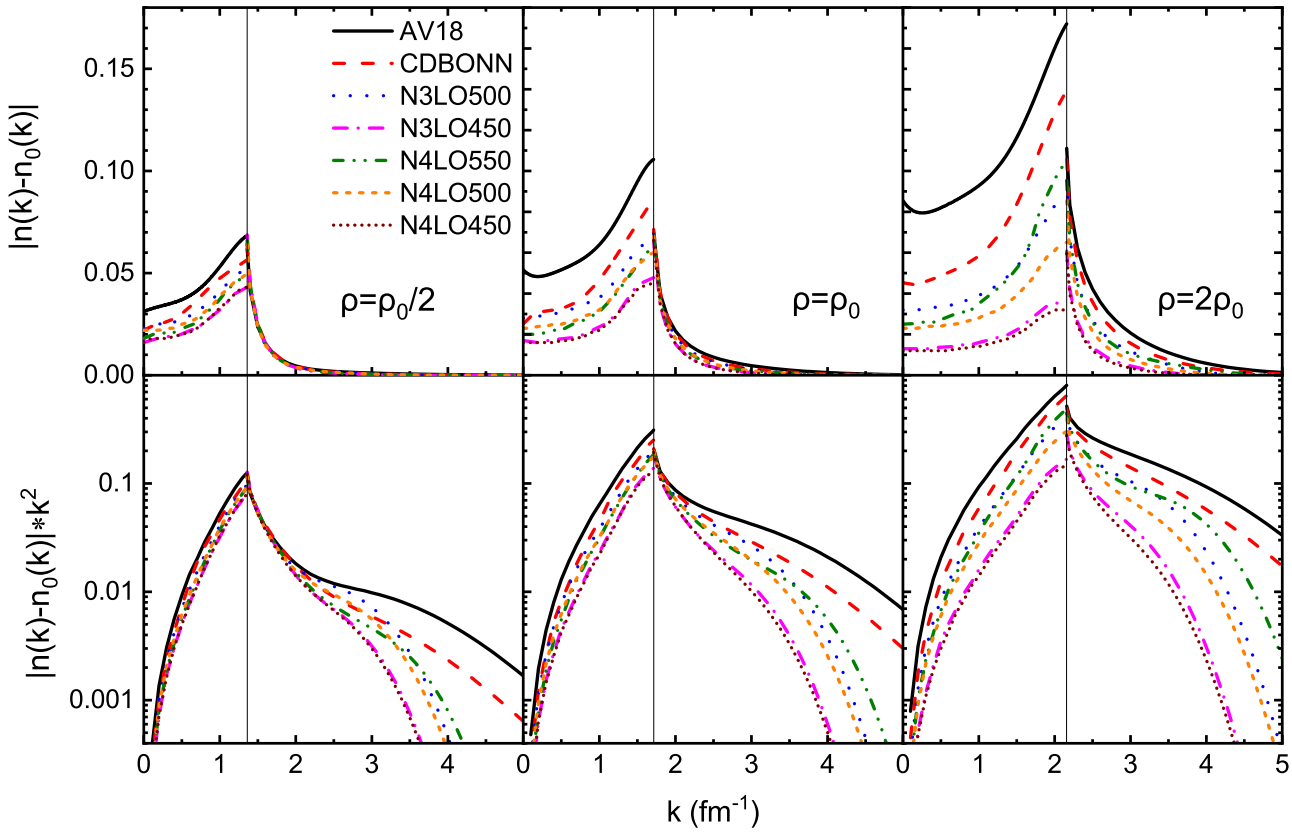

FIG. 3. Deviation of the momentum distribution in PNM from the bare Fermi distribution $n_0(k) = \theta(k_F - k)$ for all potentials at different densities ($\rho_0 = 0.17$ fm^{-3}). The bottom panels are weighted with a factor k^2 in order to emphasize the long-range tail of the distributions.

D. Correlation parameter

The hole-line parameter $\kappa(\rho) = \rho V_{\rm core}(\rho)$, computed from Eq. (2), is shown in Fig. 5. Mainly due to the absence of the $^3SD_1$ channel, it is smaller in PNM than in SNM, where values of above 0.25 are reached with the AV18 potential [3]. The hard core $V_{\rm core}(\rho)$ of the meson-exchange potentials resists well when increasing the density, and therefore κ continues to rise with increasing density. On the contrary, the absence of a hard core for the soft chiral potentials causes $V_{\rm core}(\rho)$ to shrink faster than linearly with density, and therefore also κ decreases with increasing density in this case.

The density in Fig. 5 extends to a fairly high value $\rho = 0.8$ fm^{-3}, corresponding to $k_F = 2.87$ fm$^{-1} \approx 570$ MeV, beyond the range of validity of the chiral forces. Nevertheless the density dependence of the results is regular, apart from the N4LO550 model, which features bad convergence for $\rho \gtrsim 0.5$ fm^{-3}, i.e., the BHF iterative procedure fails to have a stable solution. In any case the correlation parameter is rather small, $\kappa \lesssim 0.1$ for the chiral potentials, and therefore, since also the condition $c < d$ is well fulfilled, a very good convergence of the HLE is to be expected, which we verify now.

E. Binding energies E_2 and E_3

Figure 6 shows the binding energy per neutron obtained at second (left panel) or third (right panel) order of the HLE. We just mention that in the BHF calculations we use $J_{\rm max} = 9$ in the partial-wave decomposition and $k_{\rm max} = 7.5$ fm^{-1} for the computation of the single-particle potential $U(k)$. Just as in SNM [4], the meson-exchange potentials yield naturally more repulsion at high density, whereas the results of the chiral potentials are ordered according to their cutoff value. Indeed the N3LO and N4LO models give very similar results for the same cutoff. The largest discrepancy is about 4% at $\rho = 0.8$ fm^{-3} for the N*LO500 models with continuous choice, but much less at lower density and for the N*LO450 forces.

It is obvious that the difference between gap-choice and continuous-choice results, which is an indicator for the convergence of the expansion, is strongly reduced when going from second to third order. This indicates that the third-order (or the second-order continuous-choice) results for PNM are practically converged in the HLE up to the high densities considered here. This feature is clearly consistent with the smallness of the correlation parameter κ, as pointed out before. We give a typical example: For the AV18 at $\rho = 0.17$ fm^{-3}, the width of the error band between gap- and continuous-choice results is 1.10 and 0.21 MeV at 2HL and 3HL level, respectively. Therefore the convergence is improved by $0.21/1.1 \approx 0.2$, which is of the same order as the hole-line parameter $\kappa \approx 0.08$. For the other potentials quite similar values are obtained.

We note nevertheless that at the highest density, the error bands defined in this way do (marginally) not overlap for

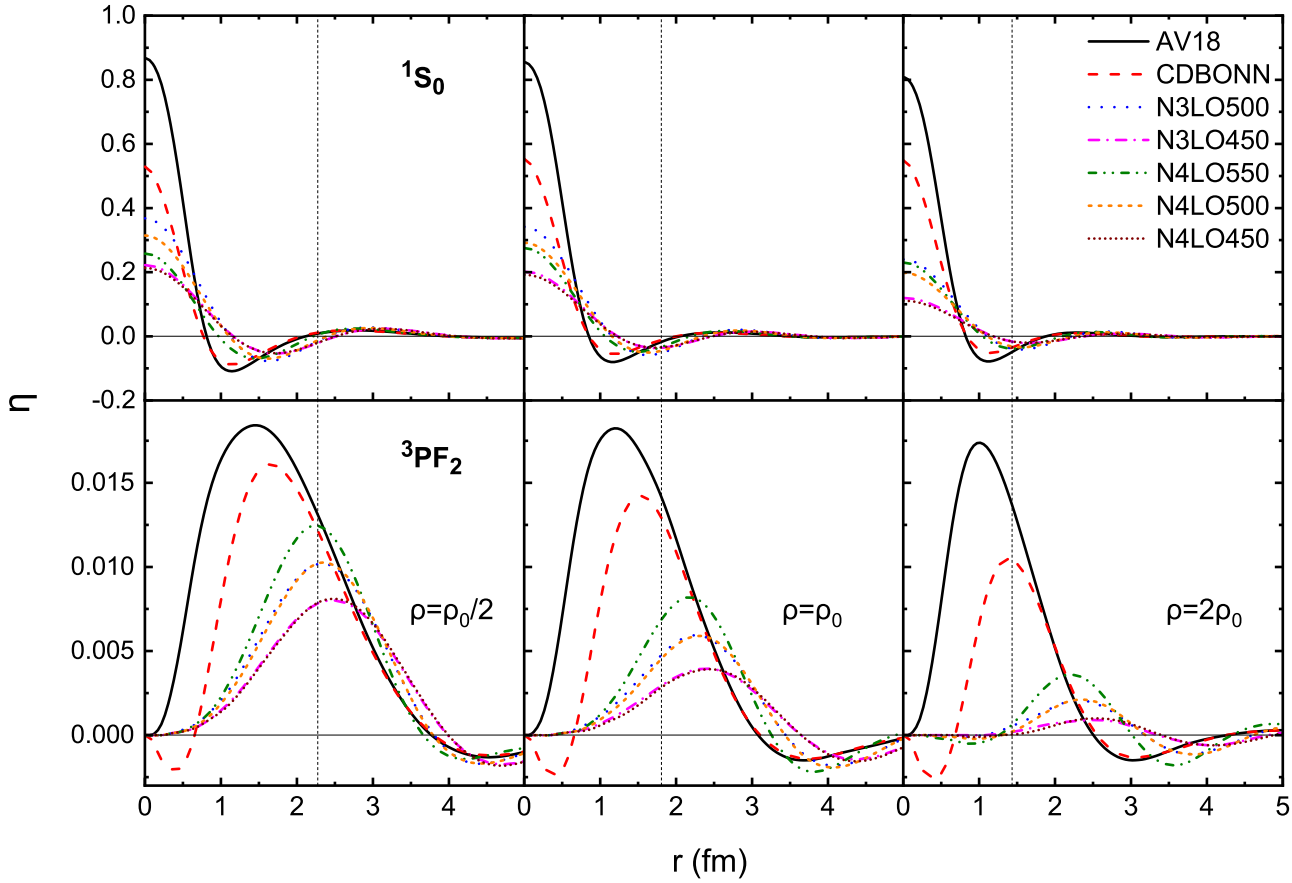

FIG. 4. $^1S_0$ and $^3PF_2$ defect functions in PNM at different densities ($\rho_0 = 0.17$ fm^{-3}) for all potentials. The vertical dashed lines indicate the interparticle distance $d \equiv \rho^{-1/3}$.

the AV18 results, which indicates that this criterion does not provide exact limits on the energy at any given order. In fact the difference between both choices is very large at 2HL level for the AV18.

On the other hand, the results (in particular at high density) depend strongly on the chosen NN potential, which means that the missing three-body forces also depend strongly on the potentials, just as in SNM, where the chiral potentials require

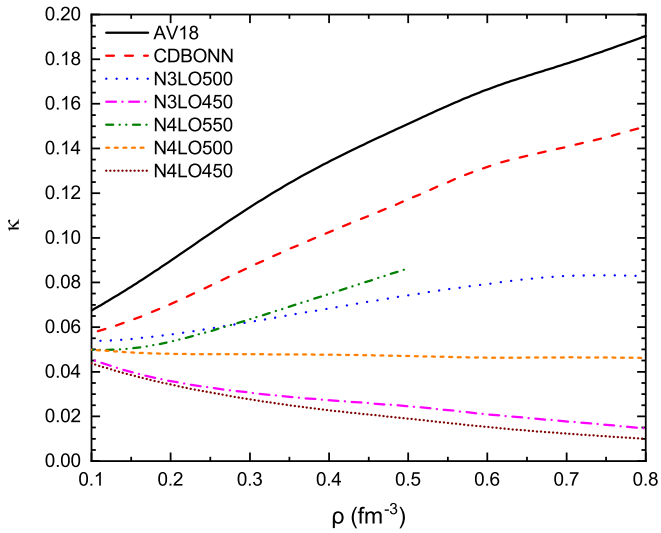

FIG. 5. Correlation parameter κ, Eq. (2), in PNM for all potentials. The N4LO550 calculations do not converge well for $\rho \gtrsim 0.5$ fm^{-3}.

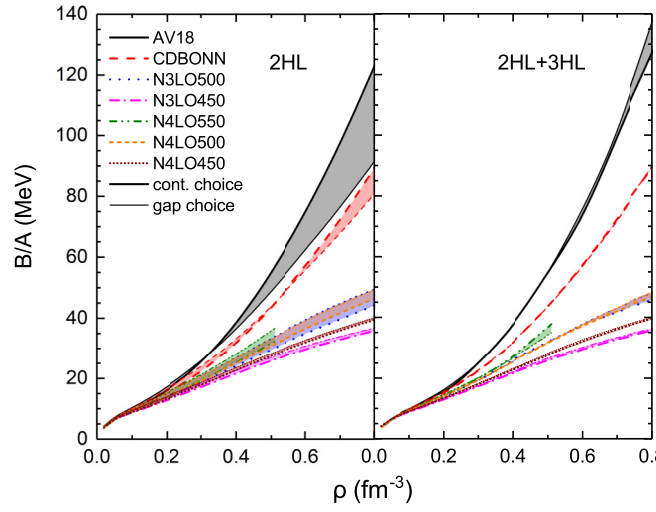

FIG. 6. Energy per particle of PNM for different NN potentials in 2HL (left panel) and 2HL+3HL (right panel) approximation with continuous- (thick curves) or gap-choice (thin curves) s.p. potentials. The N4LO550 calculations do not converge well for $\rho \gtrsim 0.5$ fm^{-3}.

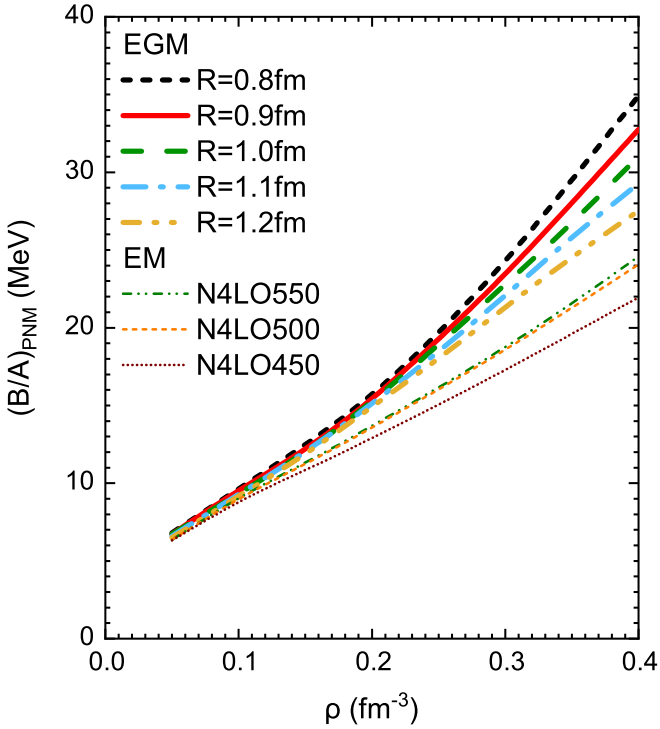

FIG. 7. Comparison of continuous-choice BHF results with N4LO EM and EGM potentials. The relation between r-space regulator and chiral cutoff is $\Lambda = 2/R$ [27,28].

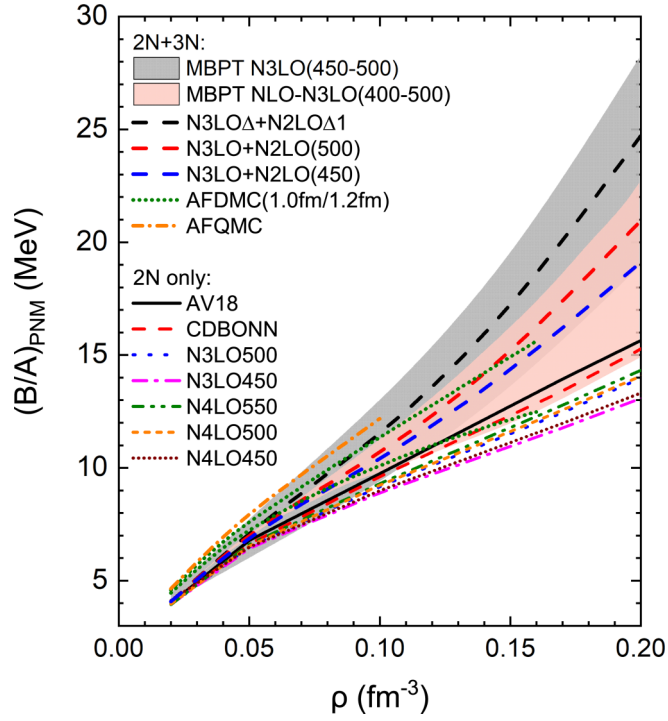

FIG. 8. Energy per particle of PNM in continuous-choice 2HL+3HL approximation for different NN potentials without 3N forces (thin curves) in comparison with other calculations, all using chiral 2N+3N forces (bold curves): many-body perturbation theory [30,31]; BHF including Δ degrees of freedom [32]; diffusion Monte Carlo [33]; quantum Monte Carlo [34].

strong three-body forces in order to provide good saturation properties of nuclear matter [4].

F. Comparison with other works

PNM has been a test bed for different theoretical computation schemes and NN interactions, and we therefore provide now a short comparison with such previous results.

Figure 7 shows the binding energy per neutron of our well-converged continuous-choice 2HL results with the N4LO EM potentials in comparison with the equivalent BHF (no TBF) results presented in Ref. [27] obtained with the EGM chiral potentials [28] of the same order N4LO. We note substantially lower values obtained with the EM potentials. Already above normal density $\rho = \rho_0$ the EM and EGM results do not coincide for any of the chosen chiral cutoffs. This confirms the important conclusion drawn in Refs. [27–29] that the residual cutoff dependence of the energy per particle does not allow for a reliable estimation of the theoretical uncertainty, which could be much larger. This would mean for PNM an uncertainty of more than 10 MeV at $\rho = 0.4$ fm^{-3} at fifth order of chiral perturbation theory (no TBF), for example.

Finally, in order to visualize the current status of theoretical calculations of PNM, Fig. 8 compares our 2HL+3HL results with those obtained in other many-body approximation schemes [30–34] (listed in the figure caption), all employing chiral 2N+3N forces, i.e., including TBF. The plot thus confirms essentially the importance of TBF, and it can be concluded that repulsive effects of TBF are required for all potentials, increasing with the softness of the interaction. Although the plot gives a qualitative assessment of the importance of TBF and current theoretical accuracies, we do stress again that the results compared in the figure are not obtained on equivalent theoretical grounds: While the two-body potentials are the same, our calculations do currently not include any TBF, whereas the other frameworks do not consider consistent 3HL corrections in a comparable way (although we have shown here that those are very small). Both items remain tasks for future improvements.

IV. CONCLUSIONS

We have carefully analyzed properties of pure neutron matter in the BBG hole-line expansion at second and third order in the correlation parameter κ. This parameter turns out to be of the order of only a few percent up to high density for all NN potentials analyzed, in particular for the chiral potentials, which together with the validity of the $c < d$ condition implies excellent convergence of the HLE. This is confirmed by explicit calculation, such that in practice the BHF results with the continuous choice of s.p potentials can be considered converged in the HLE.

The binding energy of PNM obtained in this way then depends strongly on the hard-core features of the chosen NN potentials, which implies important contributions of three-nucleon forces in particular with the chiral models. This is still a theoretical challenge for both meson-exchange and chiral NN potentials.

ACKNOWLEDGMENTS

We thank R. Machleidt for providing the chiral potentials and for useful communications. This work is sponsored by the National Natural Science Foundation of China under Grants No. 11075037, No. 11475045. We further acknowledge partial support from "PHAROS," COST Action CA16214.

[1] S. Gandolfi, A. Gezerlis, and J. Carlson, Ann. Rev. Nucl. Part. Science **65**, 303 (2015).

[2] S. Gandolfi, J. Carlson, S. Reddy, A. W. Steiner, and R. B. Wiringa, Eur. Phys. J. A **50**, 10 (2014).

[3] Z. H. Li and H.-J. Schulze, Phys. Rev. C **94**, 024322 (2016).

[4] J.-J. Lu, Z.-H. Li, C.-Y. Chen, M. Baldo, and H.-J. Schulze, Phys. Rev. C **96**, 044309 (2017).

[5] K. A. Brueckner and J. L. Gammel, Phys. Rev. **109**, 1023 (1958); J. P. Jeukenne, A. Lejeune, and C. Mahaux, Phys. Rep. **25C**, 83 (1976); B. Day, Nucl. Phys. A **328**, 1 (1979).

[6] M. Baldo, *Nuclear Methods and the Nuclear Equation of State*, International Review of Nuclear Physics, (World Scientific, Singapore, 1999), Vol. 8.

[7] M. Baldo and G. F. Burgio, Rep. Prog. Phys. **75**, 026301 (2012).

[8] R. Machleidt and D. R. Entem, Phys. Rep. **503**, 1 (2011); R. Machleidt, Symmetry **8**, 26 (2016).

[9] F. Coester, S. Cohen, B. Day, and C. M. Vincent, Phys. Rev. C **1**, 769 (1970); B. D. Day and F. Coester, *ibid.* **13**, 1720 (1976).

[10] Z. H. Li, U. Lombardo, H.-J. Schulze, W. Zuo, L. W. Chen, and H. R. Ma, Phys. Rev. C **74**, 047304 (2006).

[11] R. B. Wiringa, V. G. J. Stoks, and R. Schiavilla, Phys. Rev. C **51**, 38 (1995).

[12] R. Machleidt, Phys. Rev. C **63**, 024001 (2001).

[13] D. R. Entem and R. Machleidt, Phys. Lett. B **524**, 93 (2002); Phys. Rev. C **68**, 041001(R) (2003).

[14] D. R. Entem, R. Machleidt, and Y. Nosyk, Phys. Rev. C **96**, 024004 (2017).

[15] B. D. Day, F. Coester, and A. Goodman, Phys. Rev. C **6**, 1992 (1972); B. D. Day, *ibid.* **24**, 1203 (1981); Phys. Rev. Lett. **47**, 226 (1981).

[16] H. A. Bethe, B. H. Brandow, and A. G. Petschek, Phys. Rev. **129**, 225 (1963); B. H. Brandow, *ibid.* **152**, 863 (1966); M. W. Kirson, Nucl. Phys. A **99**, 353 (1967); B. D. Day, Rev. Mod. Phys. **39**, 719 (1967); R. Rajaraman and H. A. Bethe, *ibid.* **39**, 745 (1967).

[17] M. I. Haftel and F. Tabakin, Nucl. Phys. A **158**, 1 (1970); Phys. Rev. C **3**, 921 (1971).

[18] M. Baldo and H. R. Moshfegh, Phys. Rev. C **86**, 024306 (2012).

[19] M. Baldo, G. Giansiracusa, U. Lombardo, and H. Q. Song, Phys. Lett. B **473**, 1 (2000); M. Baldo, A. Fiasconaro, H. Q. Song, G. Giansiracusa, and U. Lombardo, Phys. Rev. C **65**, 017303 (2001).

[20] M. Baldo and C. Maieron, J. Phys. **G34**, R243 (2007).

[21] M. Baldo and C. Maieron, Phys. Rev. C **72**, 034005 (2005).

[22] M. Baldo, A. Polls, A. Rios, H.-J. Schulze, and I. Vidaña, Phys. Rev. C **86**, 064001 (2012).

[23] K. Fukukawa, M. Baldo, G. F. Burgio, L. Lo Monaco, and H.-J. Schulze, Phys. Rev. C **92**, 065802 (2015).

[24] P. Grange, J. Cugnon, and A. Lejeune, Nucl. Phys. A **473**, 365 (1987).

[25] M. Baldo, I. Bombaci, G. Giansiracusa, U. Lombardo, C. Mahaux, and R. Sartor, Nucl. Phys. A **545**, 741 (1992).

[26] W. Zuo, I. Bombaci, and U. Lombardo, Phys. Rev. C **60**, 024605 (1999).

[27] J. Hu, Y. Zhang, E. Epelbaum, Ulf-G. Meißner, and J. Meng, Phys. Rev. C **96**, 034307 (2017).

[28] E. Epelbaum, H. Krebs, and U.-G. Meißner, Phys. Rev. Lett. **115**, 122301 (2015); Eur. Phys. J. A **51**, 53 (2015).

[29] F. Sammarruca, L. Coraggio, J. W. Holt, N. Itaco, R. Machleidt, and L. E. Marcucci, Phys. Rev. C **91**, 054311 (2015).

[30] C. Drischler, A. Carbone, K. Hebeler, and A. Schwenk, Phys. Rev. C **94**, 054307 (2016).

[31] J. W. Holt and N. Kaiser, Phys. Rev. C **95**, 034326 (2017).

[32] D. Logoteta, I. Bombaci, and A. Kievsky, Phys. Rev. C **94**, 064001 (2016).

[33] I. Tews, S. Gandolfi, A. Gezerlis, and A. Schwenk, Phys. Rev. C **93**, 024305 (2016).

[34] G. Wlazlowski, J. W. Holt, S. Moroz, A. Bulgac, and K. J. Roche, Phys. Rev. Lett. **113**, 182503 (2014).